A Multilevel DC to Three-Phase AC Architecture for Photovoltaic Power Plants

Prasanta K. Achanta, *Student Member, IEEE*, Brian B. Johnson, *Member, IEEE*, Gab-Su Seo, *Member, IEEE*, and Dragan Maksimovic, *Fellow, IEEE*

***Abstract*—This paper presents a photovoltaic (PV) inverter architecture composed of stackable dc to three-phase ac converter blocks. Several such blocks, each containing a converter power stage and controls, are connected in series on their ac sides to obtain transformerless medium-voltage ac interfaces for PV power plants. The series-connected structure is made possible by a quadruple active bridge dc–dc converter that provides isolation between the PV input and each of the three ac-side phases within each block. Furthermore, since incoming PV power is transferred as constant balanced three-phase ac power, instantaneous input–output power balance bypasses the need for bulk energy storage. To streamline implementation and maximize system scalability and resilience, decentralized block-level controllers accomplish dc-link voltage regulation, maximum power point tracking, and ac-side power sharing without centralized means. The proposed architecture is validated by simulations of a PV string to medium-voltage ac system consisting of six blocks and on a proof-of-concept hardware prototype that consists of three cascaded converter blocks.**

***Index Terms*—DC-AC power converters, decentralized control, multilevel converters.**

I. Introduction

TODAY, utility-scale photovoltaic (PV) inverters are predominantly built with single-stage topologies that interface with an externally installed low-voltage to medium-voltage line-frequency transformer. Given the costs, maintenance, and power losses associated with line-frequency transformers, manufacturers are investigating transformerless architectures that produce medium-voltage ac (MVAC) directly. To achieve this aim, multilevel inverters act as a natural choice because the large number of series-connected devices not only allows for increased voltage blocking but also enables the synthesis of high-quality waveforms [1]–[4]; however, existing multilevel inverters require bulky passive components that add costs or centralized controllers that impede scalability [5]–[12]. To circumvent these shortcomings, we propose a cascaded architecture composed of interconnected blocks that are each designed to process constant power and eliminate bulk energy storage. Further, local controls within each block natively achieve both block- and system-level aims, making the system truly modular and scalable. The approach is verified by simulations of a string PV to MVAC system comprising six cascaded converter blocks and by experiments on a proof-of-concept prototype consisting of three blocks.

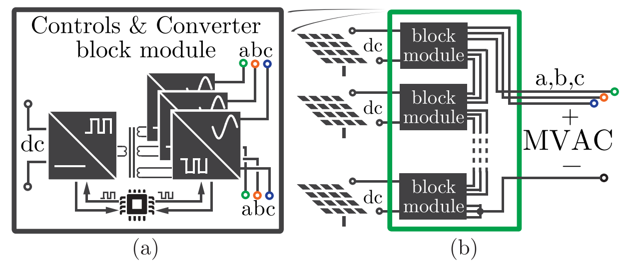

Fig. 1. The dc to three-phase ac block in (a) forms the foundation of the transformerless architecture in (b). The converter stack performs string-level MPPT on each PV string, while low-distortion waveforms are synthesized on the MVAC side.

Existing transformerless topologies for utility-scale inverters fall under the following system types: i) modular multilevel converters (MMCs) with cascaded half- or full-bridge cells [5], and ii) systems containing interconnected active-bridge converters. One limitation of the MMC for PV applications stems from the fact that the dc input voltage must exceed the peak ac voltage. Since PV string voltages are typically at or less than 1.5 kV, this necessitates an additional boost converter stage to enable a MVAC output, which adds costs and decreases efficiency. Further, since the MMC is composed of distinct phase legs that each process pulsating power, MMC cells require large capacitor banks and a centralized voltage balancing controller [13]–[15].

On the other hand, systems of active-bridge converters facilitate large voltage-conversion ratios facilitated by isolation transformers. For instance, active-bridge converters are often connected in parallel at the low-voltage PV input, and the output sides can be cascaded to produce MVAC [8], [9]. Although this acts as a key advantage over MMCs for PV systems, ex-

Manuscript received April 9, 2018; revised August 20, 2018; accepted October 1, 2018. Date of publication October 21, 2018; date of current version February 26, 2019. This work was supported in part by the National Renewable Energy Laboratory, operated by Alliance for Sustainable Energy, LLC, for the U.S. Department of Energy (DOE) under Contract No. DE-AC36-08GO28308, in part by the DOE Office of Energy Efficiency and Renewable Energy Solar Energy Technologies Office under Grants DE-EE0008346.0000 and DE-EE0000-1583, and in part by NREL's Laboratory Directed Research and Development program. Paper no. TEC-00423-2018. *(Corresponding author: Prasanta K. Achanta.)*

P. K. Achanta and D. Maksimovic are with the Department of Electrical, Computer and Energy Engineering, University of Colorado, Boulder, CO 80309-0425 USA (e-mail: prasanta.achanta@colorado.edu; maksimov@colorado.edu).

B. B. Johnson is with the Department of Electrical and Computer Engineering, University of Washington, Seattle, WA 98195 USA (e-mail: brianbj@uw.edu).

G.-S. Seo is with the Power Systems Engineering Center at the National Renewable Energy Laboratory, Golden, CO 80401 USA (e-mail: gabsu.seo@nrel.gov).

Color versions of one or more of the figures in this paper are available online at http://ieeexplore.ieee.org.

Digital Object Identifier 10.1109/TEC.2018.2877151

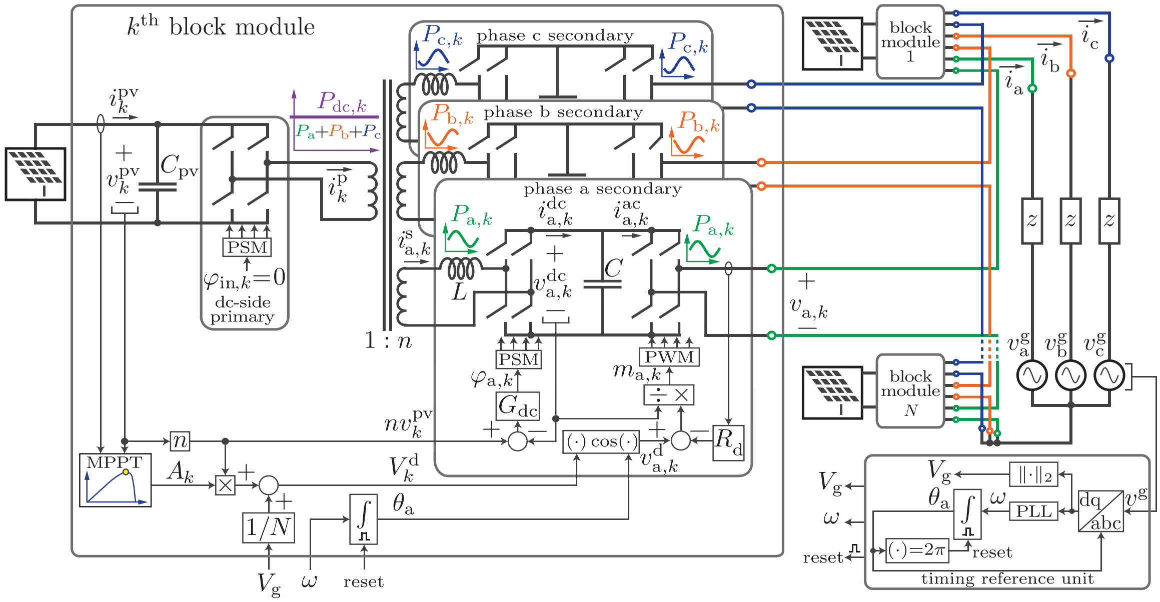

Fig. 2. The transformerless inverter system is comprised of N cascaded block modules, one subsystem that broadcasts timing reference signals, a filter impedance, and a three-phase grid. Each dc to three-phase ac power stage contains a quadruple active bridge (QAB) converter and three inverters. Each block module is autonomously controlled to perform dc-link voltage regulation, maximum power point tracking (MPPT), and droop control to ensure ac-side voltage and power balancing.

isting approaches still rely on centralized controllers [9], [16], which impede scalability and act as a single point of failure. Furthermore, depending on the type of control strategy, large dc-link capacitors may still be needed [9].

To obtain a modular, scalable and resilient system, the proposed architecture is built from fully modular blocks that have self-contained power electronics circuitry and autonomous controls, as shown in Fig. 1. The primary difference from existing active-bridge architectures is that we use a *quadruple active bridge* (QAB) [17] to simultaneously provide isolation, which enables stackability, and ensure input-output power balance, which eliminates the need for bulk energy storage. Our approach also differs from related methods [6]–[9] with QABs in that we use the QAB exclusively for isolation and restrict its operation to the “dc-transformer” (DCX) regime where the conversion ratio is close to the transformer turns ratio and efficiency is maximized [18]. Note that the QAB transformer requires medium voltage isolation between windings. Such isolation requirements are common in cascaded medium voltage architectures [6]–[9], and related transformer design approaches have been addressed in [19]–[21].

Since dc to three-phase ac conversion is accomplished within a single block, we propose a set of block-level controls to achieve system-wide objectives. In particular, we propose decentralized controllers that achieve dc-link voltage regulation, maximum power point tracking (MPPT), and power sharing across the ac stack. In summary, the contributions here are based not only on the power stage, but also on the accompanying controls that enable modular PV-to-MVAC systems without bulky line-frequency transformers.

The paper is organized as follows. The proposed system architecture is described in Section II, followed by circuit and control analysis in Section III. System validations by simulations and experiments are presented in Section IV. The paper is concluded in Section V.

II. Architecture Overview

Because of the distributed system architecture, we use vector and matrix notation where a column-vector x is denoted as $x := [x_1, \ldots, x_N]^\top$. Next, $\mathrm{diag}(x)$ denotes a matrix with diagonal entries given by the elements x and zeros elsewhere. By extension, $\mathrm{diag}^{-1}(x)$ has diagonal entries of $[x_1^{-1}, \ldots, x_N^{-1}]^\top$. A vector of length l containing all ones is given by 1_l. Three-phase quantities are compactly written as $x := [x_\mathrm{a}, x_\mathrm{b}, x_\mathrm{c}]^\top$. To facilitate analysis, switched signals averaged over a sliding window of duration T are denoted as:

$$\langle x(t) \rangle_T := \frac{1}{T} \int_{t-T/2}^{t+T/2} x(\tau) d\tau. \tag{1}$$

The overall system in Fig. 2 contains N block modules where each dc to three-phase ac converter has a dc input, a QAB dc-dc converter with $1:n$ winding ratios, and three dc-ac inverters on the output side. The dc-side of the k^{th} block module is interfaced to a PV string with voltage v_k^{pv}, and current i_k^{pv}. Next, we denote the k^{th} QAB primary bridge current as i_k^{p}, and the secondary-side a, b, and c-phase QAB bridge currents within the column-vector $i_k^{\mathrm{s}} := [i_{\mathrm{a}k}^{\mathrm{s}}, i_{\mathrm{b}k}^{\mathrm{s}}, i_{\mathrm{c}k}^{\mathrm{s}}]^\top$. The leakage inductance of each QAB secondary is denoted as L. Each corresponding block module contains three identical dc-link capacitances C, with voltages $v_k^{\mathrm{dc}} = [v_{\mathrm{a},k}^{\mathrm{dc}}, v_{\mathrm{b},k}^{\mathrm{dc}}, v_{\mathrm{c},k}^{\mathrm{dc}}]^\top$. Dc-link currents injected and extracted by the QAB-side and inverter-side, respectively, are denoted as $i_k^{\mathrm{dc}} := [i_{\mathrm{a},k}^{\mathrm{dc}}, i_{\mathrm{b},k}^{\mathrm{dc}}, i_{\mathrm{c},k}^{\mathrm{dc}}]^\top$ and $i_k^{\mathrm{ac}} := [i_{\mathrm{a},k}^{\mathrm{ac}}, i_{\mathrm{b},k}^{\mathrm{ac}}, i_{\mathrm{c},k}^{\mathrm{ac}}]^\top$, respectively. The three inverter H-bridge voltages of the k^{th}

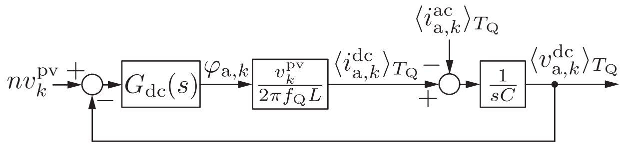

Fig. 3. Closed-loop dynamics of the phase-a subcircuit dc link within the k^{th} block module.

block are given by $v_k := [v_{\mathrm{a},k}, v_{\mathrm{b},k}, v_{\mathrm{c},k}]^\top$, and the three-phase currents delivered by the system are $i := [i_{\mathrm{a}}, i_{\mathrm{b}}, i_{\mathrm{c}}]^\top$.

The converter stack interfaces with a medium-voltage grid that we model as the balanced voltages $v^{\mathrm{g}} := [v_{\mathrm{a}}^{\mathrm{g}}, v_{\mathrm{b}}^{\mathrm{g}}, v_{\mathrm{c}}^{\mathrm{g}}]^\top$. The impedance z encapsulates the grid-side filter. A single *timing reference unit* is contained within the system and is used to broadcast the grid frequency ω, the grid voltage a-phase zero crossings (via a binary *reset* signal), and the grid voltage amplitude V_{g} to all N block modules. These signals are generated by a phase-locked loop (PLL).

The N block modules have identical control structures. Dc-side measurements are processed by the MPPT controller which in turn modulates the three-phase ac-side voltage magnitude. The QAB is controlled with three identical dc-link voltage controllers, denoted as G_{dc}. Finally, the k-th three-phase output ac side is controlled to act like sinusoidal voltage sources $v_k^{\mathrm{d}} := \left[v_{\mathrm{a},k}^{\mathrm{d}}, v_{\mathrm{b},k}^{\mathrm{d}}, v_{\mathrm{c},k}^{\mathrm{d}} \right]^\top$ behind a virtual droop resistance R_{d}.

III. Circuit and Control Analysis

A. Power-Stage Description

The four QAB bridges are controlled by phase shift modulation (PSM) where the primary bridge transistors are switched at a fixed frequency, $f_{\mathrm{Q}} = 1/T_{\mathrm{Q}}$, and 50% duty ratio. Furthermore, the rising edge of the k^{th} primary-side switch signal acts as a phase reference for its respective three secondaries where the phase shifts of the a-, b-, and c-side bridges are $\varphi_{\mathrm{a},k}$, $\varphi_{\mathrm{b},k}$, and $\varphi_{\mathrm{c},k}$, respectively. Assuming small phase shifts, the average current delivered by the a-phase secondary can be approximated as [22]:

$$\langle i_{\mathrm{a},k}^{\mathrm{dc}}(t) \rangle_{T_{\mathrm{Q}}} \approx \frac{v_k^{\mathrm{pv}} \varphi_{\mathrm{a},k}(t)}{2\pi f_{\mathrm{Q}} L}, \tag{2}$$

where expressions for b and c-phase secondary currents take correspondingly similar forms.

Fig. 2 illustrates the QAB transformer as one multi-winding transformer. However, equivalent functionality can be obtained with three distinct but identical dual-winding transformers that couple the dc side to each respective phase. Although the multi-winding implementation may yield gains in power density due to constant power transfer, the choice between one or three transformers is primarily dictated by voltage ratings and isolation requirements. For instance, because a single multi-winding transformer must withstand the peak voltage differences between each ac phase and the PV input, it will be necessary to ensure proper spacing between windings and/or insulating dielectric materials between windings.

As a consequence of the proposed dc-link control strategy (described in Section III-B), pulsating power is delivered by each QAB secondary and transferred directly to the grid-side inverters (see $P_{\mathrm{a},k}, P_{\mathrm{b},k}$, and $P_{\mathrm{c},k}$ in Fig. 2). Because of direct line-frequency energy transfer, each dc link stores constant energy and can be minimally sized to absorb just the high-frequency switching ripple. This is in contrast to existing architectures that require large dc-link capacitances to buffer line-frequency power. Since net constant balanced three-phase grid-side power is matched at all times with PV-side dc power (i.e., $P_{\mathrm{a},k} + P_{\mathrm{b},k} + P_{\mathrm{c},k} = P_{\mathrm{dc},k}$ in Fig. 2), this allows for the elimination of bulky passives within each converter.

Each grid-side H-bridge inverter is modulated via sine-triangle unipolar PWM such that each bridge provides a three-level voltage waveform. Switch interleaving among the N cascaded H-bridges in each phase is obtained by uniformly phase shifting the N carrier waveforms amongst the block modules. Here, carrier interleaving is obtained via a combination of the PLL zero-crossing reset signal, which acts as a time reference for all units, and the locally computed phase shift based on the block module index number. Accordingly, the three-phase stack voltages, $\sum_{k=1}^{N} v_k$, take on $2N+1$ levels for each ac phase, as described in [3].

Regarding system-level design, we anticipate that the number of cascaded units will be decided based on the grid voltage rating. Furthermore, the number of cascaded units and their cumulative voltage rating should be chosen with sufficient margin such that a small number of failed units can be bypassed without interrupting system operation. Last, we envision that system expansion will be done in discrete stages (add a new stack of N block modules) instead of incrementally (add one block-module to an existing stack).

B. Control Design

The timing reference unit contains a PLL that computes ω and V_{g}. A zero-crossing detector is triggered when the PLL angle, θ_{a}, crosses zero. We use a prototypical PLL that contains a compensator in closed loop with an abc-to-dq coordinate transformation [23]. Since the grid voltage, V_{g}, and frequency, ω, typically stay close to constant over any given ac cycle, the value of ω is transmitted to all N blocks only once each ac cycle along with the zero-crossing reset signal. This strategy minimizes the broadcast bandwidth requirements and eases implementation. Also note that the timing reference unit performs no module-level or system-level control functions, and that it performs only low-bandwidth unidirectional communication to the block modules, with no information needed from the block modules.

Next, consider the secondary-side QAB dc-link voltage regulators shown in Fig. 2. As illustrated, each a-, b-, and c-phase subcircuit within the k^{th} module contains an identical proportional-integral (PI) compensator, G_{dc}, that generates the phase shifts $\varphi_k := [\varphi_{\mathrm{a},k}, \varphi_{\mathrm{b},k}, \varphi_{\mathrm{c},k}]^\top$ and ensures $[v_{\mathrm{a},k}^{\mathrm{dc}}, v_{\mathrm{b},k}^{\mathrm{dc}}, v_{\mathrm{c},k}^{\mathrm{dc}}]^\top \to nv_k^{\mathrm{pv}} 1_3$. In other words, each QAB is controlled to act as a fixed $1:n$ dc transformer (DCX) where the PV voltage is reflected to each secondary dc link. This strategy is known to maximize active bridge converter efficiency by minimizing circulating currents and through the simultaneous use of zero-voltage switching [18].

The closed-loop dynamics for each dc link within the k^{th} module can be represented using Fig. 3, and the loop-gain is

$$\ell_k(s) = G_{\text{dc}}(s)\frac{v_k^{\text{pv}}}{2\pi f_{\text{Q}} L}\frac{1}{sC}. \tag{3}$$

For the sake of design, we can assume v_k^{pv} is near its nominal maximum power point (MPP) voltage and use standard linear systems analysis [24], [25] to tune $G_{\text{dc}}(s)$. The bandwidth of the dc-link controller is designed to be sufficiently higher than twice the line frequency ($\gg \frac{\omega}{\pi}$) so that the dc-link voltages are well regulated while each phase delivers single-phase ac power.

As a consequence of the dc-link control strategy, the PV input and ac grid sides are directly coupled, much like a single-stage three-phase inverter. Accordingly, PV MPPT is directly tied to the grid-side control strategy and the dc-links are controlled independently via the QAB phase shifts. To achieve autonomous power sharing among cascaded units [26], each set of ac phase terminals is modulated to track the droop-controlled average value:

$$\langle v_k \rangle_{T_{\text{H}}} = v_k^{\text{d}} - R_{\text{d}} i, \tag{4}$$

where $T_{\text{H}} = f_{\text{H}}^{-1}$ is the switching period for all H-bridges, the three-phase voltages are

$$v_k^{\text{d}} := \begin{bmatrix} v_{\text{a},k}^{\text{d}} \\ v_{\text{b},k}^{\text{d}} \\ v_{\text{c},k}^{\text{d}} \end{bmatrix} = V_k^{\text{d}} \begin{bmatrix} \cos(\theta_{\text{a}}) \\ \cos(\theta_{\text{a}} - \frac{2\pi}{3}) \\ \cos(\theta_{\text{a}} + \frac{2\pi}{3}) \end{bmatrix}, \tag{5}$$

and θ_{a} is a locally generated copy of the PLL angle within each block module. To ensure (4) is satisfied, the modulation signals for the k^{th} set of H-bridges are given by

$$m_k := \begin{bmatrix} m_{\text{a},k} \\ m_{\text{b},k} \\ m_{\text{c},k} \end{bmatrix} = \text{diag}^{-1}(v_k^{\text{dc}})(v_k^{\text{d}} - R_{\text{d}} i). \tag{6}$$

The PV-side MPPT influences grid-side power delivery by modulating the droop voltage amplitude V_k^{d}. As shown in Fig. 2, the voltage amplitude is

$$V_k^{\text{d}} = A_k n v_k^{\text{pv}} + \frac{V_{\text{g}}}{N}, \tag{7}$$

where A_k is a voltage adjustment factor produced by the MPPT. Although a variety of MPPT algorithms are compatible with this setup, we utilize a simple perturb and observe method that adjusts A_k up/down with a fixed step size, ΔA, and periodically at T_{PO} as shown in Fig. 4.

C. Steady-State System Analysis

Here we analyze how the grid-side voltage and current waveforms depend on PV-side conditions. We first consider the general case where PV string power is nonuniform among the N block modules. Lastly, we focus on the special but important case where each PV string produces identical power.

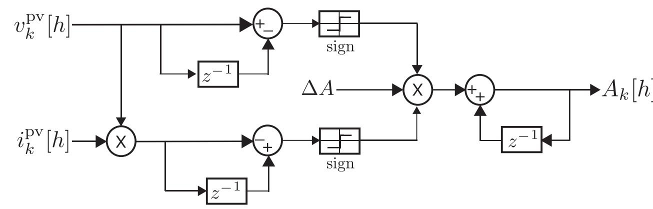

Fig. 4. A block diagram illustrating the perturb and observe MPPT algorithm.

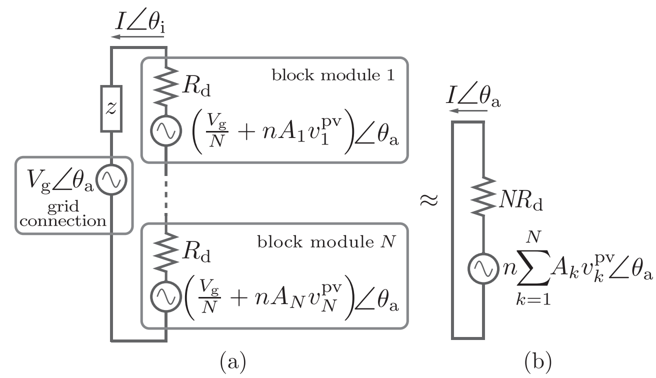

Fig. 5. One-line diagrams of the steady-state grid-side voltages and current. The representation in (a) shows each block module explicitly. After simplifying and neglecting the filter impedance, we obtain the system in (b).

The one-line phasor diagram in Fig. 5(a) shows the multi-converter cascaded architecture and its steady-state ac waveforms resulting from the grid-side droop controls. All phasor magnitudes in Fig. 5 correspond to peak values, and I denotes the ac peak current. Using (4), the amplitude of the k^{th} H-bridge terminal voltage phasor is

$$V_k = \sqrt{2\langle |v_{\text{a},k}^{\text{d}} - R_{\text{d}} i_{\text{a}}|^2 \rangle_{2\pi/\omega}}, \tag{8}$$

where the ac quantities on the right-hand side of (8) are assumed to be in sinusoidal steady state. Since the inverter filter, z, is designed to filter high-order harmonics, we can assume it has negligible impedance at the grid frequency. After neglecting z (for all analysis that follows) and summing voltages, we obtain the simplified representation in Fig. 5(b).

Nonuniform Power Delivery: Kirchhoff's laws give the following general expressions for the stack current and grid power:

$$I = \frac{n}{NR_{\text{d}}}\sum_{k=1}^{N} A_k v_k^{\text{pv}}, \quad P = \frac{3nV_{\text{g}}}{2NR_{\text{d}}}\sum_{k=1}^{N} A_k v_k^{\text{pv}} \tag{9}$$

where P denotes the power absorbed by the grid. In (9), it is evident that the output current and grid power depends on the MPPT outputs, $A_1, \ldots, A_N$, as well as the QAB turns ratio, PV voltages, and the number of modules.

From (9), the magnitude of the voltage across the k^{th} H-bridge then follows as:

$$V_k = \frac{V_{\text{g}}}{N} + nA_k v_k^{\text{pv}}\left(1 - \frac{1}{N}\right) - \frac{n}{N}\sum_{j \neq k} A_j v_j^{\text{pv}}. \tag{10}$$

We denote the efficiency of the k^{th} converter as η_k and the PV power as $P_k^{\text{pv}} := i_k^{\text{pv}} v_k^{\text{pv}}$. The conservation of energy then

TABLE I
STRING PV TO MVAC SYSTEM PARAMETERS

N	No. of block modules	6
n	Transformer turns ratio	2
ω	Grid frequency	$2\pi 50$ rad/s
v^g	Grid voltage	$[7.62, 7.62, 7.62]^\top kV_{rms}$
z	Grid side filter impedance	$[1+j\,0.314]\ \Omega$
V_{mpp}	String MPP voltage	1.05 kV
P	System power	600 kW
R_d	Virtual droop resistance	48.5 Ω
ΔA	**MPPT step size**	**0.01**

allows us to obtain the following expression, which illuminates the relationship between PV power production and grid-side voltage distribution across the stack:

$$\frac{P_j^{\mathrm{pv}}}{\sum_{k=1}^{N} P_k^{\mathrm{pv}}} = \frac{\eta_j V_j}{\sum_{k=1}^{N} \eta_k V_k} \tag{11}$$

Uniform Power Generation: In the case where all dc-side PV strings produce identical power, the general expressions in (9)–(11) simplify and yield insights into system behavior. These set of conditions should closely match those of well-designed large-scale PV plants (e.g., minimal partial shading or other mismatch factors) during nominal operation. If we let $A = A_1, \ldots, A_N$, $\eta = \eta_1, \ldots, \eta_N$ and $v^{\mathrm{pv}} = v_1^{\mathrm{pv}}, \ldots, v_N^{\mathrm{pv}}$, these relationships become

$$I = \frac{nAv^{\mathrm{pv}}}{R_{\mathrm{d}}}, \quad P = \frac{3nV_{\mathrm{g}}Av^{\mathrm{pv}}}{2R_{\mathrm{d}}}, \tag{12}$$

$$P_k^{\mathrm{pv}} = \frac{P}{\eta N}, \quad V_k = \frac{V_{\mathrm{g}}}{N}, \ \forall k. \tag{13}$$

Here, (13) demonstrates that voltage and power sharing are natively obtained via the proposed droop control method.

IV. System Validation

System operation, including operation of the dc-link controllers, string level MPP tracking, and ac-side power sharing without a central controller are verified by simulations reported in Section IV-A and experiments in Section IV-B.

A. String PV-to-MVAC System Simulations

This section describes a representative 600 kW system connected to a 13.2 kV medium-voltage grid using $N = 6$ block modules connected in series, as shown in Fig. 2. The system parameters are provided in Table I. Under nominal full-sun operating conditions, each PV string operates at MPP voltage of $v_k^{\mathrm{pv}} = 1.05$ kV, and produces 100 kW. The block modules can be realized, for example, using 1.7 kV Silicon Carbide (SiC) switches for the primary side and 3.3 kV SiC devices for the secondary-side QAB switches. The inverter switches can be realized using insulated-gate bipolar transistors (IGBT) or SiC devices. Fig. 6 shows the steady-state ac-side waveforms for the case when all block modules operate under full-sun irradiation at identical MPP voltage and power. The output voltage of the multi-converter cascaded system has $2N + 1 = 13$ levels, demonstrating multi-level operation.

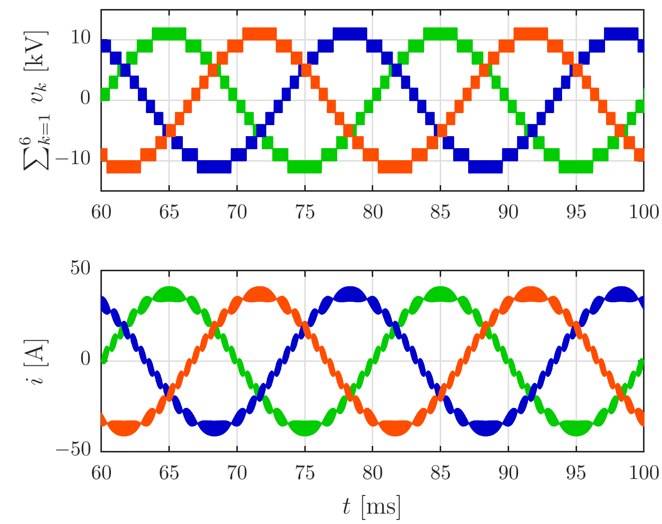

Fig. 6. Three-phase steady-state voltage and current waveforms for the 600 kW system with six block modules connected in series.

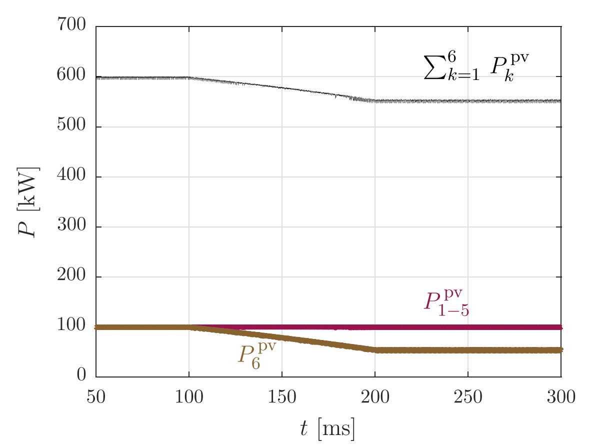

Fig. 7. System transitioning from uniform irradiation on all the PV strings to 50% shading on the PV string connected to block module #6.

To demonstrate the system's ability to operate with mismatched PV strings, Fig. 7 shows a case where initially all PV strings are operating at the same 100-kW level, followed by a 50 % reduction in solar irradiation on the PV string connected to block #6. This corresponds to a 50 kW reduction in the power processed by block module #6. The remaining PV strings and block modules continue to operate at their nominal full-sun MPP. As shown in (11) and illustrated in Fig. 8, the ac-side voltages of block modules #1–#5 increase, whereas the output voltage of block module #6 is reduced, which demonstrates autonomous proportional power sharing among the block modules. The overall system power reduction is shown in the reduced grid currents in Fig. 8(c).

To further illustrate the ability of the system to perform under extreme mismatches, simulations are performed for the case where multiple PV strings generate zero power (see Figs. 9–10). When two of six PV strings generate zero power, the voltages

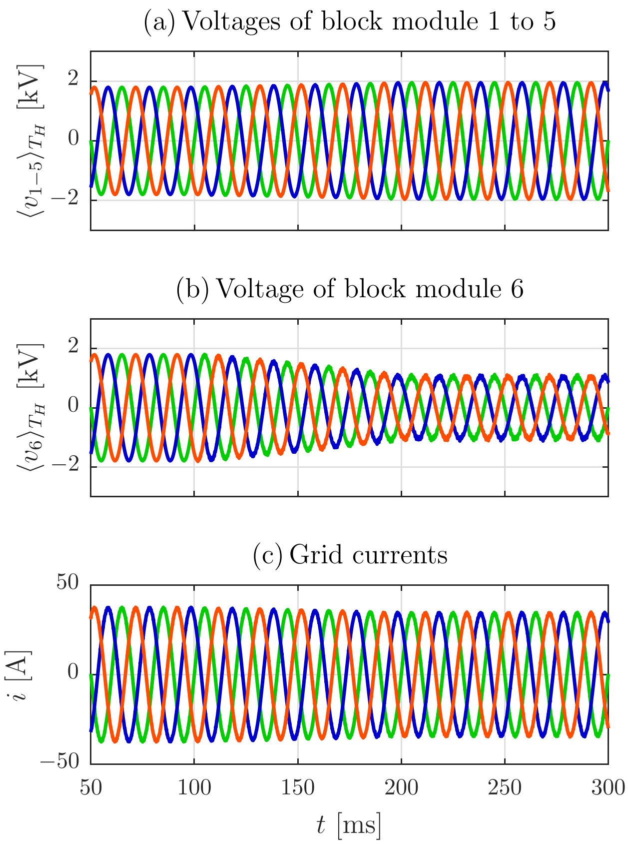

Fig. 8. Waveforms verifying autonomous and proportional power sharing operation among cascaded block modules when the system is transitioning from uniform irradiation on all the PV strings to 50% shading on the PV string connected to block module #6.

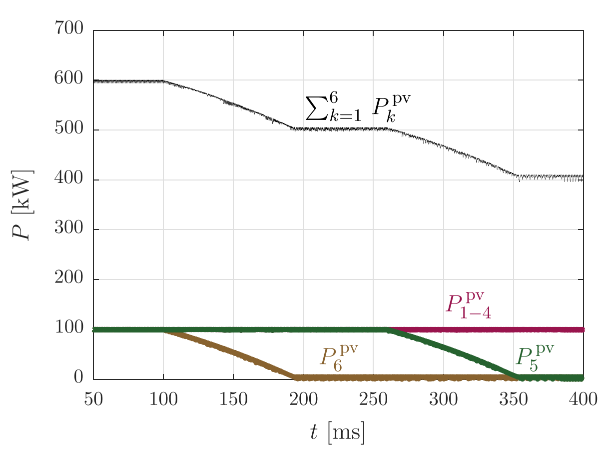

Fig. 9. System transitioning from uniform irradiation across all PV strings to zero irradiation on the PV strings connected to block module #6 followed by block module #5.

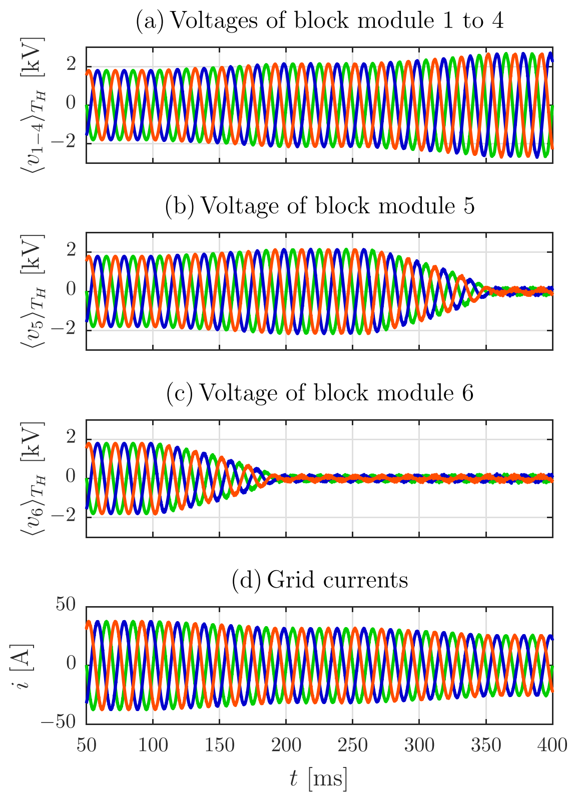

Fig. 10. Waveforms verifying autonomous and proportional power sharing operation among cascaded block modules when multiple PV strings produce zero power.

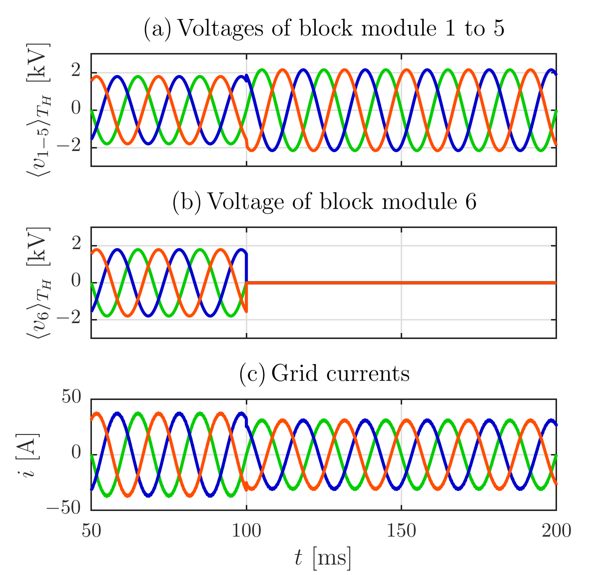

Fig. 11. Waveforms demonstrating ability of the system to maintain operation even when one of the block modules is shorted out of the system.

across those corresponding block modules are zero, and the remaining units share the grid voltage. The peak voltage across the other block modules in this extreme mismatch scenario is 2.7 kV and still within the 3.3 kV rating of the switching devices.

In the case where a failure is detected within a block, that module can be shorted while still maintaining system operation. A scenario where block module #6 is bypassed is recreated in simulation, and the resulting waveforms are shown in Fig. 11.

B. Experimental Results

A scaled proof-of-concept prototype consisting of three block modules has been constructed to verify system operation by experiments. The system parameters are summarized in Table II, and a single 250 W block module prototype is displayed in Fig. 12.

TABLE II
PARAMETERS OF THE EXPERIMENTAL PROTOTYPE

N	No. of block modules	3
f_{Q}	QAB switching frequency	100 kHz
f_{H}	H-bridge switching frequency	20 kHz
n	Transformer turns ratio	1
C_{pv}	**Input capacitance**	**90 μF**
C	Dc-link capacitance	180 μF
L	Leakage inductance	23 μH
K_{p}	Proportional gain	2.962×10^{-1} rad / V
K_{i}	Integral gain	7.5×10^{-3} rad / (V$\cdot$ s)
	MOSFETs	BSC046N10NS3 G
	Microcontroller	TMS320F28379D
	Experiments with PV module	
V_{mpp}	PV module's MPP voltage	36.8 V
z	load impedance	$[0.147\,j + (10 \parallel \text{-}289\,j)]\ \Omega$
	Standalone cascaded experiments	
v^{in}	Input voltage	40 V
z	load impedance	$[0.147\,j + (50 \parallel \text{-}289\,j)]\ \Omega$
	Grid-tied cascaded experiments	
ω	Grid frequency	$2\pi 60$ rad/s
v^{in}	Input voltage	43 V
v^{g}	Grid voltage	$[75, 75, 75]^{\top}\ V_{\mathrm{rms}}$
R_{d}	Virtual droop resistance	10 Ω
z	filter impedance	$[2 + 0.35\,j]\ \Omega$

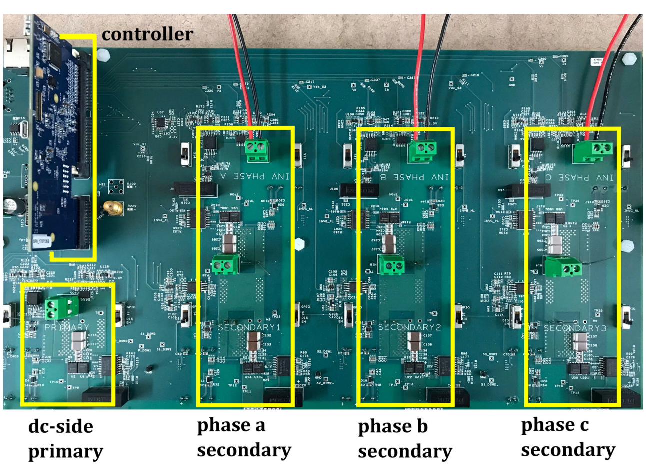

Fig. 12. A 250 W proof-of-concept prototype block module for experimental verification.

Using the prototype block modules, three sets of experimental results are provided to verify the key operational principles and feasibility. First, a single block module with PV at its input is presented to verify its fundamental functions, including dc-link regulation and MPPT operation. Next, experiments with $N = 3$ cascaded block modules demonstrate the following: parallel-input series-three-phase-output operation, multi-level voltage synthesis, and grid-tied operation with a start-up sequence. The parameters for each setup are summarized in Table II.

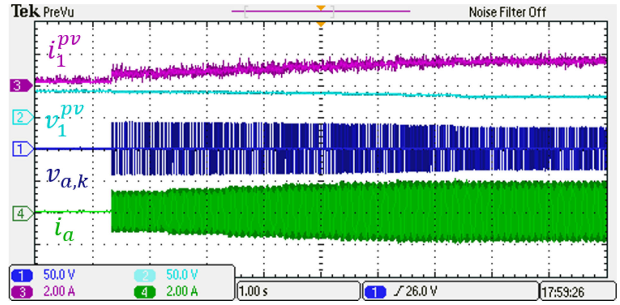

Fig. 13. System start-up operation: The PV module voltage gradually reaches the MPP voltage of 36.8 V starting from the open-circuit voltage of 43 V.

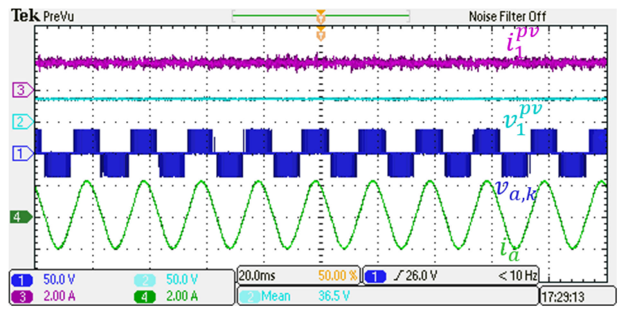

Fig. 14. Steady-state operation of a PV-powered block module delivering maximum power to a balanced three-phase load. Only phase a waveforms are shown for clarity.

Operation of Block Module With PV: We consider a single block module sourced by a PV module and connected to a balanced resistive load. Our objective is to demonstrate i) a well-defined start-up sequence, ii) dc-link voltage regulation and power balance without bulky decoupling capacitors, and iii) MPPT operation.

In this setup, a block module is sourced by a 175 W PV module with nominal MPP voltage $v^{\mathrm{pv}} = 36.8$ V. Fig. 13 illustrates start-up operation of the system. Initially, the block module is off, which allows the PV module to reach its open-circuit voltage of 43 V. Once enabled, the QAB operates as a 1:1:1:1 converter, which charges the dc-link voltages to the PV module's open-circuit voltage. It is also noteworthy that the dc link voltages are regulated under zero power transfer. The three inverters then start switching and delivering power to the three-phase load. The modulation index of the inverters is adjusted by the MPPT controller such that the PV module voltage gradually approaches the MPP voltage, as shown in Fig. 13. As illustrated in Fig. 14, the MPP is reached, and peak power is delivered to the three-phase load. By comparing the smooth dc waveforms and balanced three-phase ac waveforms on the input and output sides of the converter, it is clear that power balance is maintained.

Stand-Alone Cascaded Operation of Three Block Modules: Following the module-level MPPT demonstration, we now consider a multi-converter system with a voltage source across the inputs and a resistive ac-side load. The three block modules are connected in series, as shown in Fig. 15, and the experimental setup is shown in Fig. 16. Dc to three-phase ac conversion and

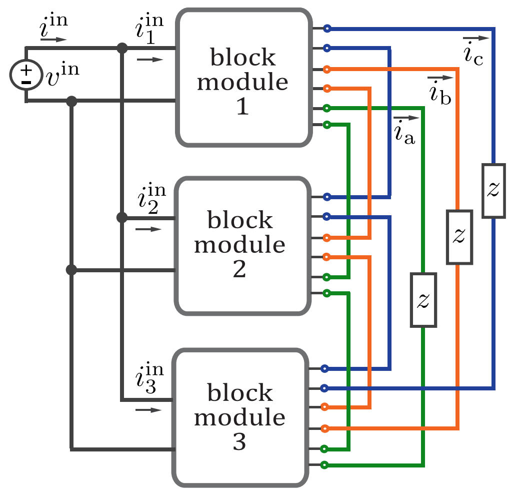

Fig. 15. Experimental setup for stand-alone operation of three block modules connected in a parallel-input series-output configuration.

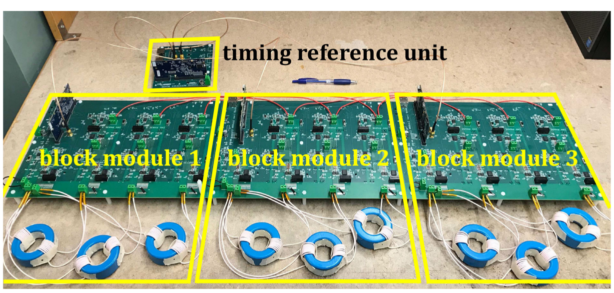

Fig. 16. Experimental setup showing three block modules connected in series along with the timing reference unit.

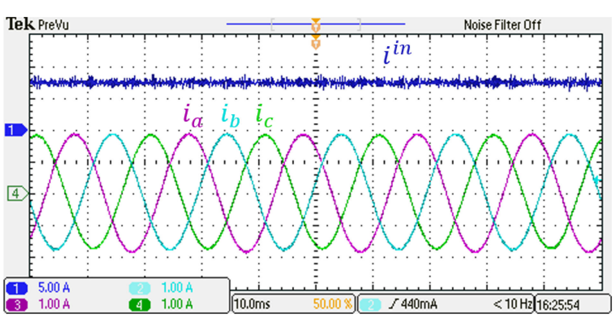

Fig. 17. DC input current and three-phase output currents of the series-stacked system with three block modules.

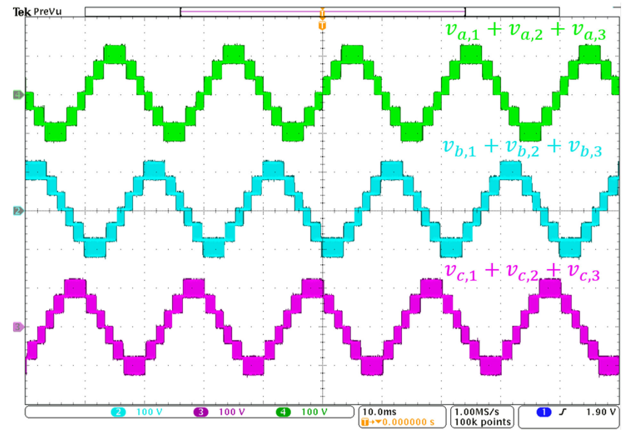

Fig. 18. Three-phase ac-side voltages of the series-stacked system demonstrating multilevel operation of the architecture. In the experiment, seven levels are synthesized using three modules.

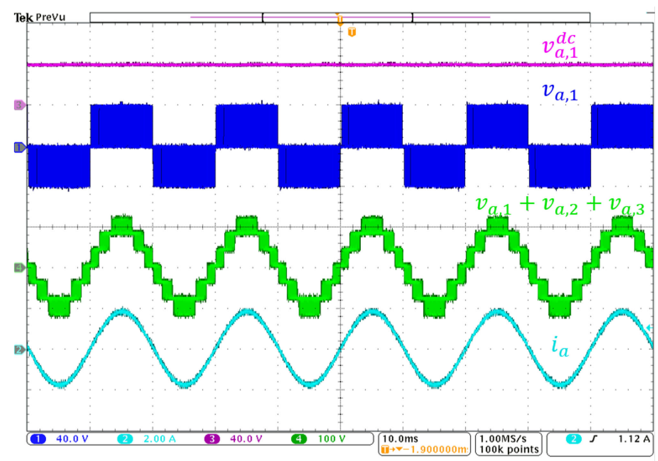

Fig. 19. Waveforms showing successful dc-link voltage regulation.

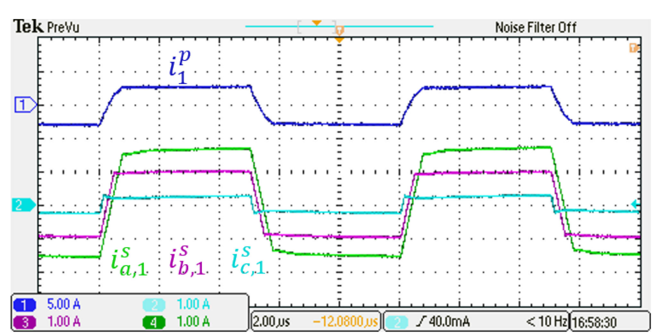

Fig. 20. Snapshot of primary and secondary transformer currents of the quadruple active bridge. The secondary currents have different phase shifts with respect to the primary current. Each independent dc-link controller determines the phase shift corresponding to each secondary.

instantaneous input-output power balance is shown in Fig. 17. Three-phase multilevel waveforms of the series-connected system are shown in Fig. 18. Since the system can exploit the series-stacked structure at the ac side by interleaving the carriers of the inverters, seven voltage levels can be synthesized with three modules.

The bandwidth of each dc-link controller is 1.6 kHz, which is sufficiently high to ensure tightly regulated voltages during most transients. Each dc-link capacitor is minimally sized since it only needs to filter switching ripple. This is illustrated in Fig. 19, which shows how the dc-link voltage of phase-a of block module #1 remains regulated during several ac line cycles. Primary and secondary QAB transformer currents at the switching timescale are shown in Fig. 20. Note how the individual secondary-side currents have different amplitudes and phase shifts, demonstrating the ability of the QAB to independently control the three dc-link voltages by phase shift modulation of the secondary bridges.

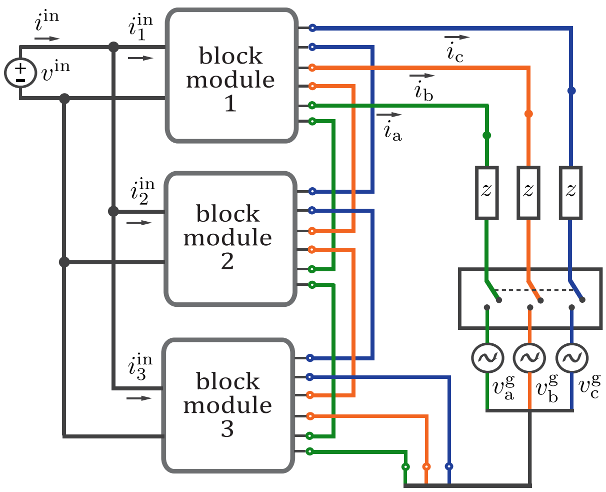

Fig. 21. Experimental system diagram for grid tied cascaded operation of three prototype block modules connected in parallel-input series-output configuration.

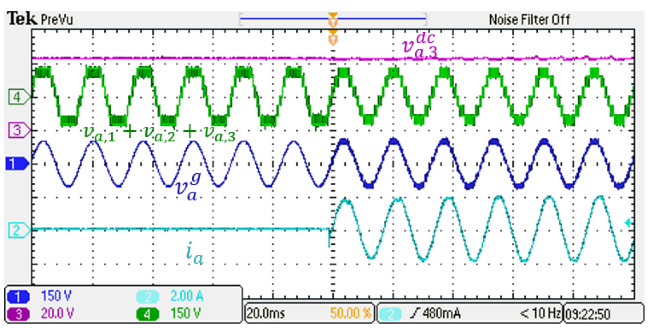

Fig. 22. Waveforms showing well regulated dc-link voltage $v_{a,3}^{\mathrm{dc}}$ during the system power ON transition. Multilevel phase-a voltage waveform across the series stack confirms $2N + 1$ levels.

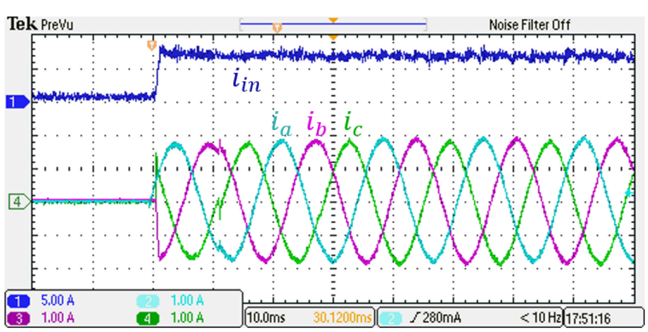

Fig. 23. System input and output currents during the turn on transient. The system transitions from no power to 300 W.

Grid-Tied Cascaded Operation: To verify grid-tied operation such as start-up, the system of three block modules is connected to a three-phase grid, as shown in Fig. 21. Since other functionalities were verified by the previous experiments, we first focus on system operation under a start-up transient and when the grid interconnect switch is closed. Fig. 22 captures the dc-link voltage of block module 3, the multilevel waveforms along with the grid voltage and grid current of phase-a under the turn on transient. As demonstrated, the multi-converter system synthesizes multi-level voltages without high bandwidth communication (only zero-crossing information from the timing reference board is needed). Multilevel operation is another key benefit since it allows us to relax ac-side filtering requirements and obtain enhanced power density. Fig. 23 shows the system input and output currents. Note that the dc-link voltage is maintained during the abrupt transition from zero ac-side power transfer in the grid-disconnected state to 300 W ac power in the grid-connected state.

V. Conclusions

We introduce a PV inverter architecture composed of stackable dc to three-phase ac converter block modules. Several such blocks, each containing autonomous controls and a converter, are connected in series on their ac sides to obtain MVAC interfaces for PV power plants without the need for bulky line-frequency transformers. Each block module consists of a quadruple active bridge (QAB) dc-dc converter and three single-phase inverters. The QAB provides isolation between the PV input and each of the three ac-side phases within each block module. Since incoming PV power is transferred as constant balanced three-phase ac power, instantaneous input-output power balance is maintained and bulk energy storage is unnecessary. A suite of controllers are proposed to ensure MPPT, dc-link voltage regulation, and ac-side voltage sharing across the stack. Taken together, the converter structure and distributed controls enable a modular and scalable system architecture. The proposed architecture is validated in a simulation of a medium-voltage 13.2 kV system and in a scaled proof-of-concept experimental prototype comprised of three 250 W block modules.

Acknowledgment

The views expressed in the article do not necessarily represent the views of the DOE or the U.S. Government.

References

[1] R. Naderi and A. Rahmati, "Phase-shifted carrier PMW technique for general cascaded inverters," *IEEE Trans. Power Electron.*, vol. 23, no. 3, pp. 1257–1269, May 2008.
[2] G. S. Konstantinou and V. G. Agelidis, "Performance evaluation of half-bridge cascaded multilevel converters operated with multicarrier sinusoidal PWM techniques," in *Proc. IEEE Conf. Ind. Electron. Appl.*, May 2009, pp. 3399–3404.
[3] B. P. McGrath and D. G. Holmes, "Multicarrier PWM strategies for multilevel inverters," *IEEE Trans. Ind. Electron.*, vol. 49, no. 4, pp. 858–867, Aug. 2002.
[4] B. Johnson, P. Krein, and P. Chapman, "Photovoltaic ac module composed of a very large number of interleaved inverters," in *Proc. Appl. Power Electron. Conf. Expo.*, Mar. 2011, pp. 976–981.
[5] S. Debnath, J. Qin, B. Bahrani, M. Saeedifard, and P. Barbosa, "Operation, control, and applications of the modular multilevel converter: A review," *IEEE Trans. Power Electron.*, vol. 30, no. 1, pp. 37–53, Jan. 2015.
[6] B. J. D. Vermulst, J. L. Duarte, C. G. E. Wijnands, and E. A. Lomonova, "Quad-active-bridge single-stage bidirectional three-phase ac-dc converter with isolation: Introduction and optimized modulation," *IEEE Trans. Power Electron.*, vol. 32, no. 4, pp. 2546–2557, Apr. 2017.
[7] H. Chen, A. Prasai, and D. Divan, "Stacked modular isolated dynamic current source converters for medium voltage applications," in *Proc. Appl. Power Electron. Conf. Expo.*, Mar. 2014, pp. 2278–2285.
[8] L. F. Costa, G. D. Carne, G. Buticchi, and M. Liserre, "The smart transformer: A solid-state transformer tailored to provide ancillary services to the distribution grid," *IEEE Power Electron. Mag.*, vol. 4, no. 2, pp. 56–67, Jun. 2017.

[9] L. F. Costa, G. Buticchi, and M. Liserre, “Quad-active-bridge dc-dc converter as cross-link for medium-voltage modular inverters,” *IEEE Trans. Ind. Appl.*, vol. 53, no. 2, pp. 1243–1253, Mar./Apr. 2017.

[10] S. Inoue and H. Akagi, “A bidirectional isolated dc-dc converter as a core circuit of the next-generation medium-voltage power conversion system,” *IEEE Trans. Power Electron.*, vol. 22, no. 2, pp. 535–542, Mar. 2007.

[11] D. Jiang, J. Xue, F. Wang, and M. H. Kao, “High density modular multilevel cascade converter for medium-voltage motor drive,” in *Proc. IEEE Elect. Ship Technol. Symp.*, Apr. 2011, pp. 482–485.

[12] H. S. Krishnamoorthy, S. Essakiappan, P. N. Enjeti, R. S. Balog, and S. Ahmed, “A new multilevel converter for megawatt scale solar photovoltaic utility integration,” in *Proc. 27th IEEE Appl. Power Electron. Conf. Expo.*, Feb. 2012, pp. 1431–1438.

[13] F. Deng and Z. Chen, “A control method for voltage balancing in modular multilevel converters,” *IEEE Trans. Power Electron.*, vol. 29, no. 1, pp. 66–76, Jan. 2014.

[14] H. Saad, X. Guillaud, J. Mahseredjian, S. DennetiÃšre, and S. Nguefeu, “MMC capacitor voltage decoupling and balancing controls,” *IEEE Trans. Power Del.*, vol. 30, no. 2, pp. 704–712, Apr. 2015.

[15] M. Hagiwara and H. Akagi, “Control and experiment of pulsewidth-modulated modular multilevel converters,” *IEEE Trans. Power Electron.*, vol. 24, no. 7, pp. 1737–1746, Jul. 2009.

[16] S. Essakiappan, H. S. Krishnamoorthy, P. Enjeti, R. S. Balog, and S. Ahmed, “Multilevel medium-frequency link inverter for utility scale photovoltaic integration,” *IEEE Trans. Power Electron.*, vol. 30, no. 7, pp. 3674–3684, Jul. 2015.

[17] P. Achanta, B. Johnson, and D. Maksimovic, “Cascaded quadruple active bridge structures for multilevel dc to three-phase ac conversion,” in *Proc. IEEE Appl. Power Electron. Conf. Expo.*, Mar. 2018, pp. 156–160.

[18] H. Chen, K. Sabi, H. Kim, T. Harada, R. Erickson, and D. Maksimovic, “A 98.7 $\%$ efficient composite converter architecture with application-tailored efficiency characteristic,” *IEEE Trans. Power Electron.*, vol. 31, no. 1, pp. 101–110, Jan. 2016.

[19] Y. A. Wang, D. M. Xiao, and Y. L. Liu, “Design of a planar power transformer for high voltage, high frequency use,” in *Proc. IEEE PES T D*, Apr. 2010, pp. 1–6.

[20] T. Guillod, J. E. Huber, G. Ortiz, A. De, C. M. Franck, and J. W. Kolar, “Characterization of the voltage and electric field stresses in multi-cell solid-state transformers,” in *Proc. IEEE Energy Convers. Congr. Expo.*, Sep. 2014, pp. 4726–4734.

[21] M. Leibl, G. Ortiz, and J. W. Kolar, “Design and experimental analysis of a medium-frequency transformer for solid-state transformer applications,” *IEEE J. Emerg. Sel. Topics Power Electron.*, vol. 5, no. 1, pp. 110–123, Mar. 2017.

[22] M. N. Kheraluwala, R. W. Gascoigne, D. M. Divan, and E. D. Baumann, “Performance characterization of a high-power dual active bridge dc-to-dc converter,” *IEEE Trans. Ind. Appl.*, vol. 28, no. 6, pp. 1294–1301, Nov./Dec. 1992.

[23] R. Teodorescu, M. Lissere, and P. Rodriguez, *Grid Converters for Photovoltaic and Wind Power Systems*. New York, NY, USA: Wiley, 2011.

[24] G. Franklin, J. Powell, and A. Emami-Naeini, *Feedback Control of Dynamic Systems*, 5th ed. Upper Saddle River, NJ, USA: Prentice-Hall, 2005.

[25] L. Corradini, D. Maksimovic, P. Mattavelli, and R. Zane, *Digital Control of High-Frequency Switched-Mode Power Converters*. Piscataway, NJ, USA: Wiley, 2015.

[26] P. Achanta, M. Ilic, and D. Maksimovic, “Decentralized control of series stacked bidirectional dc-ac modules,” in *Proc. Appl. Power Electron. Conf. Expo.*, Mar. 2018, pp. 1008–1013.

Prasanta K. Achanta (S’10) received the B.E. degree in electronics and communication engineering from Osmania University, Hyderabad, India, in 2012, and the M.S. degree in electrical engineering from the University of Colorado, Boulder, CO, USA, in 2014. From Spring 2015, he is working toward the Ph.D. degree with the Department of Electrical, Computer and Energy Engineering, University of Colorado, Boulder, CO. His research interests include design, modeling and control of power electronic converters for automotive, aerospace and renewable energy applications.

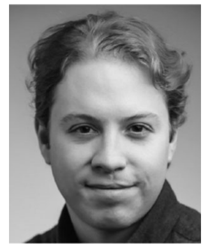

Brian B. Johnson (S’08–M’13) received the M.S. and Ph.D. degrees in electrical and computer engineering from the University of Illinois at Urbana-Champaign, Urbana, IL, USA, in 2010 and 2013, respectively. He is the Washington Research Foundation Innovation Assistant Professor with the Department of Electrical and Computer Engineering, University of Washington, Seattle, WA, USA. Prior to joining the University of Washington in 2018, he was an Engineer with the National Renewable Energy Laboratory, Golden, CO, USA. His research interests are in renewable energy systems, power electronics, and control systems. He was awarded a National Science Foundation Graduate Research Fellowship in 2010, and currently serves as an Associate Editor for the IEEE TRANSACTIONS ON ENERGY CONVERSION.

Gab-Su Seo (S’10–M’15) received the B.S. degree from Chonnam National University, Gwangju, South Korea, in 2008, and the M.S. and Ph.D. degrees in electrical engineering from Seoul National University, Seoul, South Korea, in 2010 and 2015, respectively. From 2016 to 2017, he was a Postdoctoral Researcher with the Colorado Power Electronics Center, University of Colorado, Boulder, CO, USA. Since 2018, he has been a Research Engineer with the Power Systems Engineering Center, at the National Renewable Energy Laboratory, Golden, CO, USA. His research interests include power electronics for renewable energy systems and microgrids, hybrid power conversion using wide bandgap semiconductors and switched-capacitors, and power systems engineering for grid modernization.

Dragan Maksimovic (M’89–SM’04–F’15) received the B.S. and M.S. degrees in electrical engineering from the University of Belgrade, Belgrade, Serbia (Yugoslavia), in 1984 and 1986, respectively, and the Ph.D. degree from the California Institute of Technology, Pasadena, CA, USA, in 1989. From 1989 to 1992, he was with the University of Belgrade. Since 1992, he has been with the Department of Electrical, Computer and Energy Engineering, University of Colorado, Boulder, CO, USA, where he is currently a Professor and Co-Director of the Colorado Power Electronics Center. He has coauthored more than 250 publications and the textbook Fundamentals of Power Electronics. His current research interests include power electronics for renewable energy sources and energy efficiency, high-frequency power conversion using wide bandgap semiconductors, digital control of switched-mode power converters, and analog, digital, and mixed-signal integrated circuits for power management applications. He was the recipient of the 1997 National Science Foundation CAREER Award, the IEEE Power Electronics Society (IEEE PELS) Transactions Prize Paper Awards in 1997 and 2016, the IEEE PELS Prize Letter Awards in 2009 and 2010, the University of Colorado Inventor of the Year Award in 2006, the IEEE PELS Modeling and Control Technical Achievement Award for 2012, the Holland Excellence in Teaching Awards in 2004, 2011, and 2018, the Charles Hutchinson Memorial Teaching Award for 2012, and the 2013 Boulder Faculty Assembly Excellence in Teaching Award.